Anal Bioanal Chem (2015) 407:2301–2309
DOI 10.1007/s00216-015-8460-5

RESEARCH PAPER

Subcellular-level resolution MALDI-MS imaging of maize leaf metabolites by MALDI-linear ion trap-Orbitrap mass spectrometer

Andrew R. Korte · Marna D. Yandeau-Nelson · Basil J. Nikolau · Young Jin Lee

Received: 1 December 2014 / Accepted: 5 January 2015 / Published online: 25 January 2015

Abstract A significant limiting factor in achieving high spatial resolution for matrix-assisted laser desorption ionization-mass spectrometry (MALDI-MS) imaging is the size of the laser spot at the sample surface. Here, we present modifications to the beam-delivery optics of a commercial MALDI-linear ion trap-Orbitrap instrument, incorporating an external Nd:YAG laser, beam-shaping optics, and an aspheric focusing lens, to reduce the minimum laser spot size from ~50 μm for the commercial configuration down to ~9 μm for the modified configuration. This improved system was applied for MALD I-MS imaging of cross sections of juvenile maize leaves at 5-μm spatial resolution using an oversampling method. A variety of different metabolites including amino acids, glycerolipids, and defense-related compounds were imaged at a spatial resolution well below the size of a single cell. Such images provide unprecedented insights into the metabolism associated with the different tissue types of the maize leaf, which is known to asymmetrically distribute the reactions of C4 photosynthesis among the mesophyll and bundle sheath cell types. The metabolite ion images correlate with the optical images that reveal the structures of the different tissues, and previously known and newly revealed asymmetric metabolic features are observed.

Keywords Mass spectrometry imaging · Metabolite · Maize

Published in the topical collection *Mass Spectrometry Imaging* with guest editors Andreas Römpp and Uwe Karst.

Electronic supplementary material The online version of this article (doi:10.1007/s00216-015-8460-5) contains supplementary material, which is available to authorized users.

A. R. Korte · Y. J. Lee (✉)
Department of Chemistry, Iowa State University, Ames, IA 50011, USA
e-mail: yjlee@iastate.edu

A. R. Korte · B. J. Nikolau · Y. J. Lee
Ames Laboratory-USDOE, Ames, IA 50011, USA

M. D. Yandeau-Nelson
Department of Genetics, Development and Cell Biology, Iowa State University, Ames, IA 50011, USA

B. J. Nikolau
Roy J. Carver Department of Biochemistry, Biophysics and Molecular Biology, Iowa State University, Ames, IA 50011, USA

B. J. Nikolau
Center for Metabolic Biology, Iowa State University, Ames, IA 50011, USA

Introduction

A number of factors influence and limit the spatial resolution in mass spectrometry imaging (MSI). These include tissue preparation (potential damage to the tissue or delocalization of endogenous compounds), matrix application (homogeneity of the matrix), sampling size (the area from which compounds are desorbed, ionized, and analyzed in a single spectrum), and sensitivity (sufficient detection of compounds of interest at the reduced sampling volumes of high-resolution imaging).

Tissue preparation considerations can largely be addressed by flash-freezing, cryosectioning, and lyophilizing samples after harvesting [1]. Sublimation-vapor deposition, developed by Hankin et al., has become a common method for depositing organic matrices for matrix-assisted laser desorption ionization (MALDI)-MSI and yields a homogeneous matrix coating with very small crystal sizes (1 μm or smaller [2]). In the case of inorganic matrices, an oscillating capillary nebulizer [3, 4] can be used to achieve matrix homogeneity of 10 μm or less. By definition, high-spatial resolution imaging requires

sampling of a smaller region of tissue for each individual pixel. This reduced sampling volume results in fewer ions per pixel and thus decreased sensitivity. Modern mass analyzers are extremely sensitive with almost single-ion detection capability [5], and the limitation in sensitivity is now mostly the result of insufficient ionization and ion transmission. The sampling size for each pixel is therefore the single most significant factor that restricts the spatial resolution of MALDI-MSI.

There are two types of MSI that differ in how spatial information is registered for each pixel: microscope mode and microprobe mode [6]. In microscope mode, sampling is performed for a large area at a time, the ions maintain their spatial information as they fly through the mass analyzer, and the original location of each ion is determined by a 2D microarray detector. In this mode, the spatial resolution is determined by the detector's pixel size, but the current detectors have limitations in simultaneously detecting the arrival time and the pixel position [7]. In microprobe mode, a focused laser beam scans over the sample tissue and the analytes are detected from each point separately. In this mode, the spatial resolution is limited by the laser spot size. Early work by Spengler and Hubert achieved an extremely small laser spot size of about 1 μm [8] but sacrificed ion signals by replacing ion optics with laser optics. As a result, they did not have sufficient sensitivity for biological applications. Hence, most of the more recent work has sought to utilize commercial instruments without modifying the ion optics. Spengler's group has recently developed an atmospheric pressure MALDI source capable of imaging at a spatial resolution of about 3 μm [9]. In this configuration, the laser-focusing lens was placed close to a MALDI plate outside the vacuum and the ions were transported to the detector through a capillary bored through the center of the lens.

For conventional vacuum MALDI-MSI, high spatial resolution has been demonstrated using a laser spot size down to about 10 μm [3, 10]. Most recently, Caprioli's group modified the laser optics of a commercial MALDI-time-of-flight mass spectrometer to improve the spatial resolution from the manufacturer-specified 20 μm to 5 μm [11, 12]. The improvements incorporated laser beam expansion combined with filtering of non-Gaussian beam profile components using a pinhole. Using a similar approach, Kettling et al. achieved 10-μm spatial resolution in an ion mobility-quadrupole time-of-flight mass spectrometer (Waters Synapt G2-S) [13]. In another approach, Caprioli's group also achieved 1–2 μm laser spot size using a transmission geometry laser ablation [14, 15]. Using a laser beam focused from the back side of the tissue placed on a glass slide, they demonstrated subcellular-level MSI for a few targeted immunolabeled antibodies.

The oversampling method is another way of obtaining high spatial resolution using a laser spot size larger than the desired imaging resolution. In this method, laser ablation is performed to completely remove the matrix on each pixel and the sample stage is moved at a raster step size smaller than the laser spot size. In this case, the spatial resolution is determined by the raster step size, instead of the laser spot size. Sweedler et al. demonstrated 25-μm spatial resolution using a laser beam profile that is approximately 100 μm×200 μm in size [16]. However, oversampling has been found to sacrifice sensitivity and resolution in MALDI-MS imaging experiments [11, 16]; therefore, it is still desirable to minimize the laser spot size, with oversampling providing an option for further improvement in resolution once the practical spot size limit is reached.

In the work described herein, we adapted the instrument modification concept of Caprioli [11, 12] and incorporated the modified laser optics into a MALDI-linear ion trap (LIT)-Orbitrap mass spectrometer. This resulted in an improvement of the laser spot size, from the original configuration of ~50 μm to a scale of ~9 μm. We demonstrate this improved capability of the instrument with the MSI of plant metabolites in maize leaves in 5-μm spatial resolution using the oversampling method. As a C4 plant, maize engages in a photosynthetic process that is asymmetrically distributed across two distinct cell types, mesophyll and bundle sheath cells. This unique anatomy localizes certain photosynthesis-related enzymes (and thus metabolites) to one cell type or the other [17]. Proteomics studies have established this asymmetry between the two cell types, suggesting additional metabolite distribution differences should be observable [18]. Here, we demonstrate the localization of metabolites in the cross section of juvenile maize leaves at the resolution of at least a single cell and possibly at the level of subcellular resolution using the modified instrument.

Experimental

Materials

1,5-Diaminonaphthalene (DAN, 97 %) and 2,5-dihydroxybenzoic acid (DHB, 98 %) were purchased from Sigma-Aldrich (St. Louis, MO, USA). A 355-nm frequency-tripled Nd:YAG laser (model UVFQ) was purchased from Elforlight, Ltd. (Daventry, UK). Optical components including cage rods, support plates, optical element mounts, laser line mirrors (NB1-K08), dichroic mirror (HBSY13), quartz window (WG41050), aspheric singlet (A220TM-A), spherical singlet (LA1509-A), and UV achromatic doublet (ACA254-100-UV) were purchased from Thorlabs (Newton, NJ, USA). A high-energy 25-μm pinhole (HEA-25C-R) was purchased from Lenox Laser, Inc (Glen Arm, MD, USA).

Plant growth and sample preparation

Maize seeds (*Zea mays* L., inbred B73) were planted in soil and grown under controlled conditions in a greenhouse. Healthy seedlings were selected 14 days after planting, and the third true leaf was harvested during daylight (1:00 p.m. local time). A ~2-cm portion was cut from the midpoint of the leaf. Image features shown in this manuscript were reproducibly observed across leaves from multiple seedlings under similar experimental conditions.

Embedding and sectioning were conducted using the procedure previously described [19]. Briefly, samples were submerged in gelatin and rapidly frozen in liquid nitrogen. Transverse sections were cut at 10 μm thickness using a cryostat (Leica CM1850, Leica Microsystems, Buffalo Grove, IL, USA). Due to the fragility of the tissue, it was necessary to use adhesive tape windows to collect the sections. To avoid any metabolite delocalization or loss of material, the tissue was left attached to the tape throughout matrix application and data acquisition. After cutting, tissue sections were gradually warmed and dried under moderate vacuum (~100 mtorr or 0.13 mBar). Matrix (DAN) was applied by sublimation (~50 mtorr (0.067 mBar), 140 °C, 3.5 min heating time). An in-depth description of the sublimation procedure is available elsewhere [20]. A tissue section adjacent to the one used for MALDI-MSI was used to collect an optical microscope image.

Mass spectrometry analysis

MALDI-MSI was performed using a MALDI-linear ion trap-Orbitrap mass spectrometer (MALDI-LTQ-Orbitrap Discovery; Thermo Scientific, San Jose, CA, USA) [21]. Tune and Xcalibur (Thermo Scientific) software were used to define imaging acquisition parameters. Images were acquired at a raster step size of 5 μm. The laser pump diode current was set to 80.5 % of maximum, resulting in an output energy of ~1–1.5 μJ/pulse. Each spectrum was acquired with ten laser shots, and a single spectrum was collected at each raster point. Spectra were acquired in negative mode using the Orbitrap analyzer at the mass resolution setting of 30,000 and a scan range of m/z 100–1000. After data acquisition, images were generated using ImageQuest software (Thermo Scientific). Images were created with a m/z width of ±0.005 and were normalized to the total ion count for each pixel.

After imaging, tandem MS spectra for selected compounds were acquired manually on an adjacent tissue section. Ten scans were averaged from a region of tissue where the ion of interest was found in the imaging experiment. MS/MS spectra were acquired in the ion trap analyzer, and collision energies were individually adjusted for each analyte.

Safety warning Replacement of the manufacturer's enclosed laser system with an external laser as described here results in a class IIIB laser system, and appropriate precautions should be taken, including the use of protective eyewear and appropriate access controls.

Results and discussion

Optical modification

A description of the MALDI source design for the MALDI-LIT-Orbitrap is available elsewhere [21]. The diffraction-limited spot size for a focused laser beam is defined by the following equation [11]:

$$D_s = M^2 \cdot \frac{4}{\pi} \cdot \lambda \cdot \frac{f}{D_b}$$

where D_s, M^2, λ, f, and D_b represent diffraction-limited spot size, beam quality factor (1 for a perfect Gaussian shape), wavelength, focal length, and input beam diameter, respectively.

One can therefore minimize the laser spot size by minimizing M^2 (optimizing the beam shape), minimizing f (placing the focusing lens as close to the sample as possible), and maximizing D_b (expanding the laser beam before the focusing lens). In case that the laser incident angle (θ) is non-zero to the surface normal, the spot size is slightly larger; $D_s' \sim D_s/\cos\theta$. In the MALDI source used in our instrument, the use of a long-focal-length lens was necessary for final focusing (i.e., large f) because of the placement of the ion optics. Therefore, in this work, we concentrated primarily on improving the beam shape (the M^2 term) and expanding the beam prior to focusing (the D_b term). This was achieved by the installation of a spatial filter/beam expander in the laser optical path. The focusing lens, originally a spherical singlet, was replaced with a UV-optimized aspheric doublet to minimize the effect of optical aberrations, which can limit the achievable spot size.

A schematic representation and a photograph showing the modified optical system are presented in Fig. 1a, b, respectively. The original nitrogen laser of the MALDI source is bypassed, and an external Nd:YAG laser is used for desorption/ionization. The purpose of most optical components is straightforward. A few important components include the beam expander that contains a pinhole for spatial filtering (*4–6*) and the final focusing lens (*10*). The spatial filter focusing lens (aspheric lens with f=11.0 mm; *4*) and pinhole (25 μm high-damage threshold pinhole; *5*)

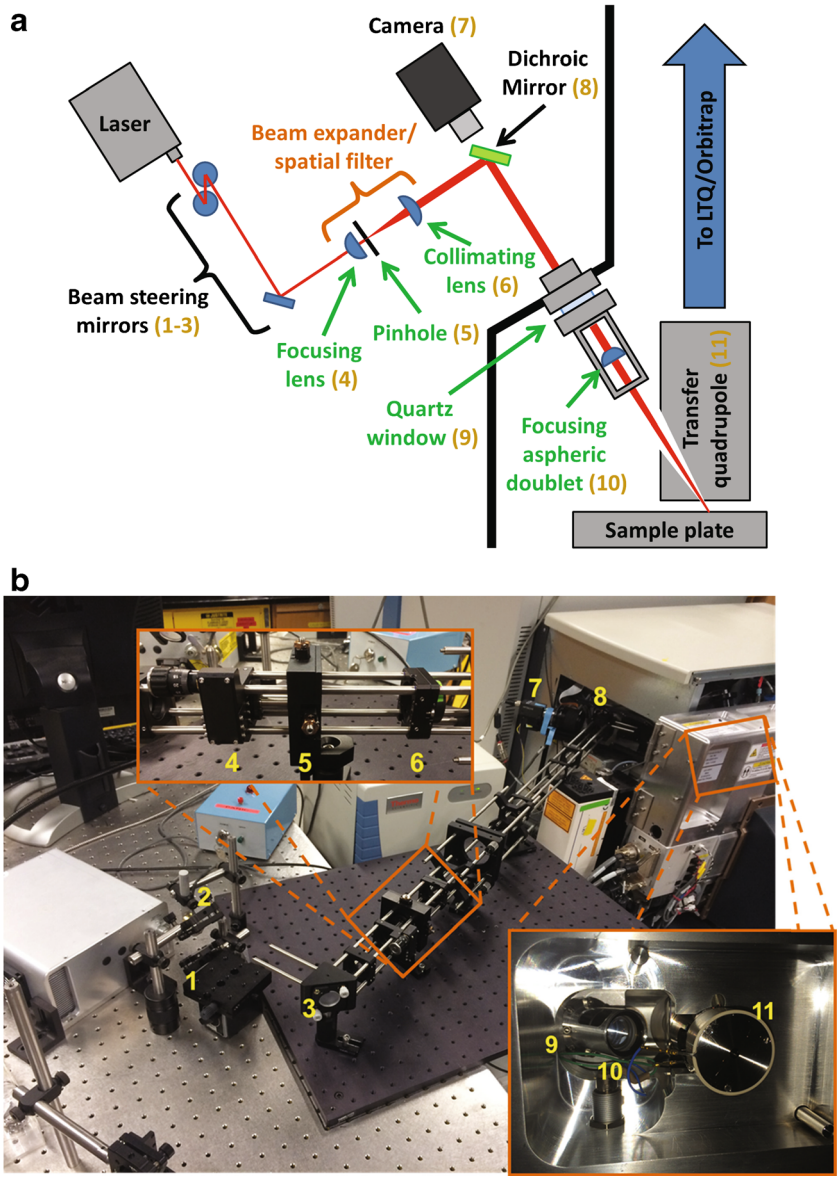

Fig. 1 **a** Schematic of modified beam-delivery optics. **b** Photographs of modified beam-delivery optics

were positioned to optimize laser transmission and beam shape. The position of the collimating lens (spherical lens with f=100 mm; *6*) was adjusted to produce a well-collimated output from the spatial filter assembly. The laser beam diameter is ~1.2 mm at the input of the spatial filter/beam expander and ~11 mm at the output. To allow for adjustments of the position of the final focusing lens, a quartz window (*9*) was installed to isolate the in-source vacuum from the atmosphere, and the final focusing lens (an aspheric doublet lens with f=100 mm; *10*) was mounted on a threaded expansion holder. The position for the final focusing lens was optimized by systematic adjustment of the lens position and measurement of the resulting ablation spots on a thin film of DHB matrix on a glass slide. The lens was fixed at the position yielding the smallest ablation spot.

Laser spot size measurement

The minimum achieved laser spot size, as estimated by the size of the ablation spot, was ~5 μm in diameter at the laser energy of 79 % (Fig. 2a). This is the expected outcome for the current focal length, beam diameter, laser wavelength, and incident angle (D_s' ~4.9 μm with M^2 ~1, f=100 mm, D_b ~11 mm, λ=355 nm, θ=32°). However, this laser energy is just above the minimum threshold needed to produce ions and did not provide a sufficient and stable ion signal for endogenous metabolites. Hence, the laser energy was increased to 80.5 % to achieve reasonable and consistent ion signals. Due to the Gaussian energy profile of the beam, increasing the energy also increases the ablation spot size. At this energy, the spot size was ~9 μm (Fig. 2b). However, room remains to further decrease the laser spot size by reducing the final focal

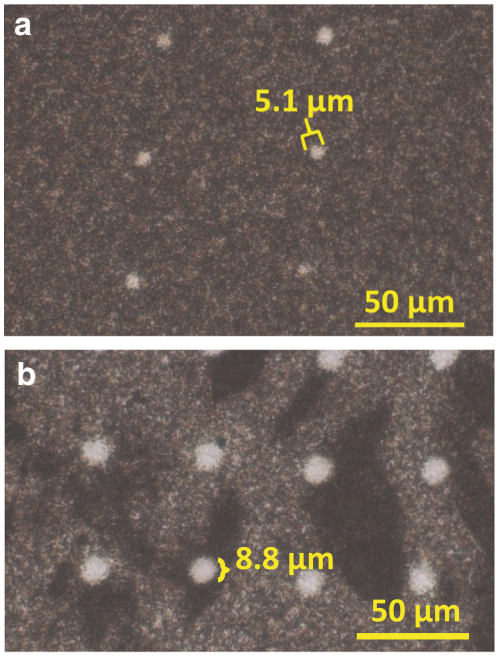

Fig. 2 Optical micrograph of laser ablation spots on a thin film of 2,5-dihydroxybenzoic acid matrix. **a** Minimum spot size at a laser energy of 79 %. **b** Practical spot size at a laser energy of 80.5 %

length to 75 mm and increasing the beam diameter to 15 mm, the approximate physical limits without significant modification of the ion source. In this configuration, we should be able to achieve a laser spot size as small as 2.7 µm; with the elevated laser energy required for imaging, we expect that this would result in an analytically practical laser spot size of ~5 µm.

In the current study, an imaging experiment was performed at 5 µm resolution with the laser spot size of ~9 µm (laser energy of 80.5 %) using an oversampling approach [16]. While this may not give as high-quality data compared to a 5-µm laser spot size, these experiments demonstrated that 5-µm high spatial resolution can be achieved by replacing the stock laser and modifying laser optics in a commercial MALDI-LIT-Orbitrap platform. Complete matrix ablation is a key for the successful implementation of the oversampling method. We used sublimation to produce a very thin matrix layer, and both visual inspection and subsequent interrogation with the laser indicate the matrix is completely ablated at each pixel.

Maize leaf imaging

Maize uses a C4 photosynthetic carbon-fixing mechanism that relies on a unique cellular anatomy, known as Kranz anatomy [22]. In this wreath-like cellular organization (*Kranz* is the German for wreath), two morphologically and functionally distinct photosynthetic cell types are arranged in concentric rings surrounding the vascular bundles. The bundle sheath cells form a single-layer inner ring that encircles each vein, and the mesophyll cells surround the bundle sheath layer. A layer of non-photosynthetic epidermal cells then encloses the upper and lower surfaces of the leaf. MALDI-MS imaging was performed on cross sections of the third leaf from maize seedlings. The presence of key metabolites and their cellular distributions were similar across leaves from multiple seedlings, and therefore, cross sections from a representative leaf are presented herein.

A collection of MALDI-MS images generated from a cross section of a juvenile maize leaf is presented in Fig. 3; an optical microscope image of the scanned region of tissue is shown as a comparison. The significantly higher spatial resolution afforded by the new optical setup allows for the distinction of much finer molecular features that are revealed by the metabolite images. These features are more visible relative to one another by overlaying MS images, as in Fig. 4. An optical image of the entire leaf section mounted on the MSI stage is presented in the Electronic Supplementary Material, Figure S1, showing the region where MSI data was acquired.

Metabolites representing a wide range of chemical classes were successfully imaged, including amino acids (glutamic acid), ascorbic acid, phenolics (caffeic acid, ferulic acid), benzoxazinone derivatives (2,4-dihydroxy-7-methoxy-1,4-benzoxazin-3-one glucoside [DIMBOA-Glc], 2-hydroxy-7-methoxy-1,4-benzoxazin-3-one glucoside [HMBOA-Glc]), sugars and phosphate sugars (hexose disaccharide, hexose phosphate), flavonoids, and flavonoid glycosides (luteolin/kaempferol, quercetin, maysin, and rutin), and glycerolipids (phosphatidylglycerol, PG (34:2), and sulfoquinovosyl diacylglycerol, SQDG (34:3)). Assignments are based upon accurate mass measurements (Electronic Supplementary Material, Table S1), but many of these chemical identities were further supported by separate MS/MS measurements performed on an adjacent tissue section (Electronic Supplementary Material, Figure S2). Nonetheless, the large number of isomers for many of these metabolites precludes an unequivocal identification, even with accurate mass and tandem MS measurements, and some signals (as discussed below) likely arise from multiple isomers.

The occurrence of structural isomers offers specific challenges in MSI experiments, as separation is solely based on mass discrimination. For example, the ion signal at *m*/*z* 285.040 can arise from either kaempferol or luteolin; the two compounds yield $[M-H]^-$ ions with an identical chemical formula ($C_{15}H_9O_6^-$) and cannot be distinguished based on accurate mass determinations. However, these metabolites are distinguishable and identifiable via MS/MS spectra. By comparing MS/MS spectra acquired from the tissue to available literature, their co-occurrence could be inferred. Fabre et al., who also used an ion trap mass spectrometer to perform MS/MS, identified the fragment ions at *m*/*z* 217 and 175 as unique to luteolin, and *m*/*z* 229 ion as unique to kaempferol

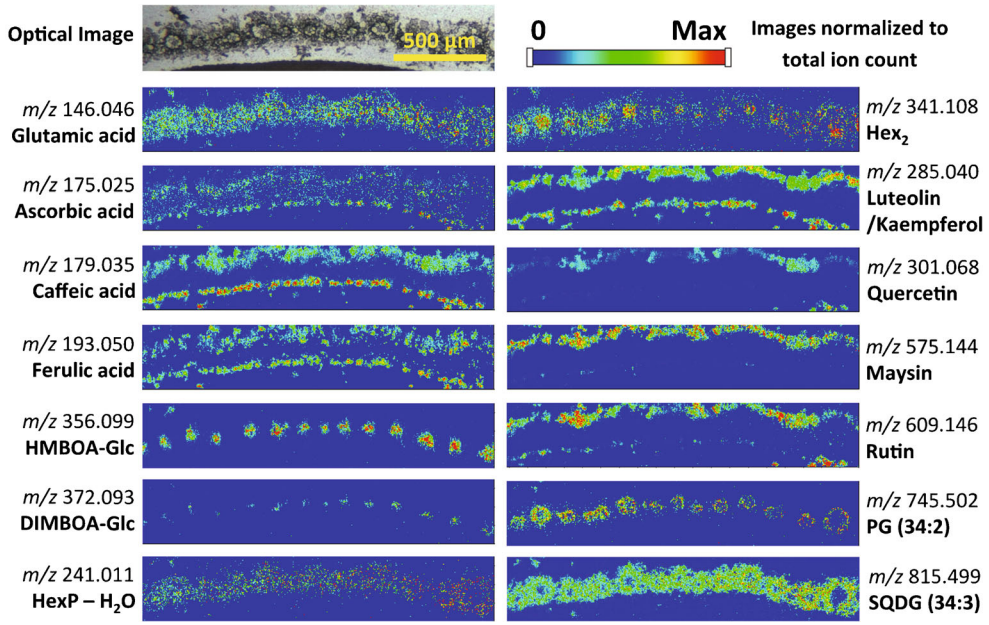

Fig. 3 Optical image and MS images of various metabolites in a maize leaf cross section obtained at 5-µm spatial resolution. Images are oriented such that the upward-facing (adaxial) surface of the leaf is at the top. *HMBOA-Glc* 2-hydroxy-7-methoxy-1,4-benzoxazin-3-one glucoside, *DIMBOA-Glc* 2,4-dihydroxy-7-methoxy-1,4-benzoxazin-3-one glucoside, *HexP* hexose phosphate, Hex_2 hexose disaccharide, *PG* phosphatidylglycerol, *SQDG* sulfoquinovosyl diacylglycerol. Signals are normalized to TIC on each pixel. Maximum values for generating images are as follows: glutamic acid, 1×10^{-2}; ascorbic acid, 8×10^{-3}; caffeic acid, 3.5×10^{-2}; ferulic acid, 8×10^{-3}; HMBOA-Glc, 3×10^{-2}; DIMBOA-Glc, 1×10^{-2}; HexP-H_2O, 4×10^{-3}; Hex_2, 6×10^{-3}; luteolin/kaempferol, 5×10^{-2}; quercetin, 4.5×10^{-2}; maysin, 5×10^{-2}; rutin, 2×10^{-2}; PG (34:2), 5×10^{-3}; SQDG (34:3), 3×10^{-2}

[23]. The presence of all three peaks in our MS/MS spectrum (Supplementary Figure 2) indicates that the parent ion at *m/z* 285.040 originates from a mixture of the two isomers.

As intermediates of central metabolism, glutamic acid and hexose phosphate (e.g., glucose-6-phosphate) are detected almost everywhere, with little cellular-level asymmetry (Fig. 3). Even though disaccharides (e.g., sucrose) may be thought of as intermediates of central metabolism, the observed distribution is very different from that of glutamic acid and hexose phosphate, being highly concentrated in the vasculature of the leaf. This latter finding is consistent with the role of sucrose as the primary sugar for moving carbon among the different organs of the plant through the phloem cells of the vasculature [24].

Metabolites that may be considered as intermediates or products of specialized metabolism are asymmetrically distributed among the leaf tissues, and this asymmetry sometimes appears to be unrelated to the common metabolic origins of

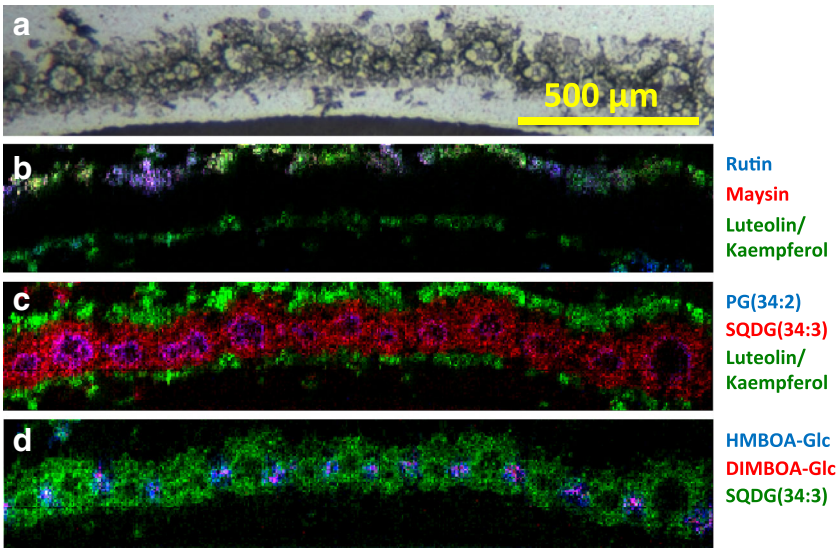

Fig. 4 The overlaid MALDI-MS images of a few compounds shown in Fig. 3

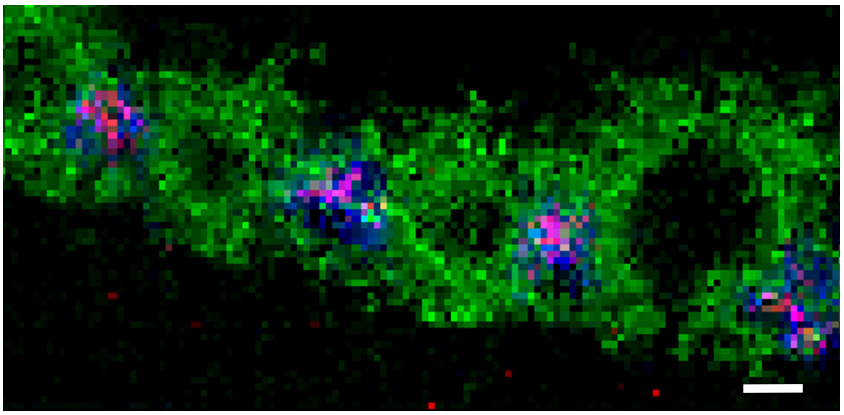

Fig. 5 Zoomed-in image of Fig. 4d. The *scale bar* corresponds to 50 μm

the metabolites. For example, the phenolics caffeic acid and ferulic acid show a very similar distribution as may be expected by the fact that they share a common metabolic origin. Specifically, they are derived from the metabolism of the amino acid phenylalanine via the phenylpropanoid biosynthetic pathway [25]. These phenolics are building blocks of a number of different plant biochemical structures, most abundant of which is probably the lignin component of plant cell walls. The distribution of caffeic and ferulic acids is near identical to each other, with a clear concentration in the cells of the lower epidermis and a more amorphous concentration in the upper epidermis and the mesophyll cells immediately adjacent.

In contrast, the five flavones that were imaged (luteolin/kaempferol, quercetin, rutin, and maysin) share common metabolic origins [26] but show varied distributions among the different cell types of the maize leaf. Luteolin, kaempferol, and quercetin are flavone aglycones, and maysin is the glycosylated form of luteolin, while rutin is the glycosylated form of quercetin. Figure 4b compares the distribution of the flavone metabolites: rutin (blue), maysin (red), and luteolin/kaempferol (green), which highlights their common localization in the upper epidermis and varied distribution in the lower epidermis. The distribution of luteolin/kaempferol is relatively homogeneous throughout the upper and lower epidermal cell layers, which is also evident in the heat map style image shown in Fig. 3. Maysin is detected almost exclusively on the upper epidermal layer, which is consistent with its anti-insect herbivory [27] and UV protectant properties [28], but its abundance varies among those cells. The flavone rutin is primarily localized to the upper epidermis and the abundance variation is similar to maysin, but it is also detected in the lower epidermal cell layer, as especially evident on the bottom right corner of the image. High rutin content in the upper epidermis compared to the lower epidermis is also reported for cotyledons of buckwheat (*Fagopyrum esculentum*) [29].

Figure 4c compares the distribution of two specific lipids that are associated with photosynthetic thylakoid membranes [30] and differ in their head groups and fatty acid components: the phospholipid PG (34:2) in blue and the sulfolipid SQDG (34:3) in red. PG (34:2) is detected in narrow (~30–40 μm) bands around the vascular bundles within the single layer of bundle sheath cells, while SQDG is detected in both bundle sheath and mesophyll cells. As both lipids are present in the bundle sheath cells (Fig. 3), this layer appears purple in color in Fig. 4c. Accordingly, the red color outside the bundle sheath layer, where SQDG is exclusively detected, corresponds to the mesophyll cells. Both PG and SQDG are known to be major components of all thylakoid membranes, and the 34:2 and 34:3 forms of PG and SQDG, respectively, have been previously demonstrated to be highly abundant in maize leaves at the developmental stage that was sampled in this study [31, 32]. In the maize leaves harvested from 45-day-old plants, SQDG has been reported to be at similar abundance in both mesophyll and bundle sheath cells, regardless of its fatty acid composition, whereas PG is asymmetrically distributed depending on its fatty acyl chains [33]. As far as we are aware, there are no reports about the cellular-level asymmetric distribution of PG in juvenile maize leaves. As shown in Supplementary Figure 3, our data suggest PG (32:0), PG (34:2), and PG (34:3) are more abundant in the bundle sheath cells, while PG (32:1) and PG (34:4) are more abundant in the mesophylls. These findings are in good agreement with the report for old leaves [33], except that they reported PG (34:2) and PG (34:3) have two combinations of fatty acyl groups that have opposite cellular distributions. Namely, Nishihara et al. reported PG (18:1/16:1) and PG (18:2/16:1) are more abundant in mesophylls and PG (18:2/16:0) and PG (18:3/16:0) are more abundant in bundle sheath cells. The fact that PG (34:2) and PG (34:3) are more abundant in bundle sheath in our data may suggest that the C16:0 fatty acyl group is dominant compared to C16:1 in the tissue samples we used. Roughan et al. reported the differential distribution of fatty acid composition across the maize leaves; i.e., the C16:1 fatty acyl group in PG is almost absent in the emerging portion of maize leaves whereas C16:0 is most dominant [31].

Figure 4d displays DIMBOA-Glc in red, HMBOA-Glc in blue, and SQDG (34:3) in green. Benzoxazinoids are

anti-herbivory defense compounds and insect deterrents [34–36]. They are stored as glucosides within the vacuole but are enzymatically released by plastidic glucosidase upon tissue maceration during the chewing of insects on leaf tissue. Enzymatic production of another benzoxazinoid, 2-hydroxy-4,7-dimethoxy-1,4-benzoxazin-3-one glucoside (HDMBOA-Glc), is triggered by chewing insects [34] and was not detected in this study (Electronic Supplementary Material, Figure S4). HMBOA-Glc and DIMBOA-Glc are co-localized between the two vascular bundles, as shown in purple in Fig. 4d. The biological foundation and implications of their localization to specific mesophyll cells between the vascular bundles are not immediately clear, but warrant further investigation.

Their spatial positioning, especially for DIMBOA-Glc, is virtually non-overlapping (or minimally overlapping) with SQDG, more evident in the zoomed-in image shown in Fig. 5. This is in good agreement with the subcellular localization of DIMBOA-Glc within the vacuole [37], as compared to SQDG, which is a chloroplast membrane lipid [38]. These findings suggest that some level of subcellular localization is possible in MSI with 5-μm resolution. Careful superimposition with high-quality optical images would be necessary to clearly assign metabolites to visually identifiable subcellular organelles and compartments. In this experiment, we used an adhesive tape to collect leaf cryosections because the leaf tissues are very fragile and other tissue fixation methods were not compatible with subsequent MSI. Unfortunately, high-quality optical imaging could not be obtained with the tissues attached to the adhesive tape.

Conclusions

We have modified the laser beam-delivery optics of a MALDI-LIT-Orbitrap mass spectrometer to produce an ablation spot size as small as 5 μm; however, to achieve sufficient ion signals, the analytically practical laser spot size was about 9 μm. Using an oversampling method, we have successfully achieved 5-μm spatial resolution MS images for cross sections of maize leaves and demonstrated cellular and subcellular distribution of a few representative metabolites. The localization of these compounds is unprecedented, and further studies will lead to a deeper understanding of the biological implication of such distribution knowledge. Further development is currently in progress to narrow the practical laser spot size to 5 μm, with which we should be able to obtain higher-quality data with better contrast. This high spatial resolution capability will be applied to the study of different tissue types for understanding plant metabolic processes at the cellular and subcellular levels of localization.

The 5-μm spatial resolution achieved and demonstrated in this work is unprecedented with this type of instrument (MALDI-LIT-Orbitrap), and only two groups have achieved such high resolution in other types of instruments [9, 11, 14]. In the current proof-of-concept experiment, we used only the negative ion mode because many of the small-molecule metabolites can be readily ionized and visualized in the negative ion mode. In future studies, we will include the positive ion mode for a comprehensive understanding of the photosynthetic and metabolic biology of maize.

Acknowledgments This work was supported by the US Department of Energy (DOE), Office of Basic Energy Sciences, Division of Chemical Sciences, Geosciences, and Biosciences. MDY-N acknowledges the support of the National Science Foundation under Award No. EEC-0813570 and Award No. IOS-1354799, which co-sponsored the development of the genetic stocks imaged in this study. The Ames Laboratory is operated by Iowa State University under DOE Contract DE-AC02-07CH11358.

References

1. Stoeckli M, Staab D, Schweitzer A (2007) Compound and metabolite distribution measured by MALDI mass spectrometric imaging in whole-body tissue sections. Int J Mass Spectrom 260(2–3):195–202. doi:10.1016/j.ijms.2006.10.007
2. Hankin JA, Barkley RM, Murphy RC (2007) Sublimation as a method of matrix application for mass spectrometric imaging. J Am Soc Mass Spectrom 18(9):1646–1652. doi:10.1016/j.jasms.2007.06.010
3. Jun JH, Song Z, Liu Z, Nikolau BJ, Yeung ES, Lee YJ (2010) High-spatial and high-mass resolution imaging of surface metabolites of Arabidopsis thaliana by laser desorption-ionization mass spectrometry using colloidal silver. Anal Chem 82(8):3255–3265. doi:10.1021/ac902990p
4. Chen Y, Allegood J, Liu Y, Wang E, Cachon-Gonzalez B, Cox TM, Merrill AH Jr, Sullards MC (2008) Imaging MALDI mass spectrometry using an oscillating capillary nebulizer matrix coating system and its application to analysis of lipids in brain from a mouse model of Tay-Sachs/Sandhoff disease. Anal Chem 80(8):2780–2788. doi:10.1021/ac702350g
5. Makarov A, Denisov E (2009) Dynamics of ions of intact proteins in the Orbitrap mass analyzer. J Am Soc Mass Spectrom 20(8):1486–1495. doi:10.1016/j.jasms.2009.03.024
6. Chughtai K, Heeren RM (2010) Mass spectrometric imaging for biomedical tissue analysis. Chem Rev 110(5):3237–3277. doi:10.1021/cr100012c
7. Soltwisch J, Goeritz G, Jungmann JH, Kiss A, Smith DF, Ellis SR, Heeren RMA (2014) MALDI mass spectrometry imaging in microscope mode with infrared lasers: bypassing the diffraction limits. Anal Chem 86(1):321–325. doi:10.1021/ac403421v
8. Spengler B, Hubert M (2002) Scanning microprobe matrix-assisted laser desorption ionization (SMALDI) mass spectrometry: instrumentation for sub-micrometer resolved LDI and MALDI surface analysis. J Am Soc Mass Spectrom 13(6):735–748. doi:10.1016/s1044-0305(02)00376-8
9. Roempp A, Guenther S, Schober Y, Schulz O, Takats Z, Kummer W, Spengler B (2010) Histology by mass spectrometry: label-free tissue characterization obtained from high-accuracy bioanalytical imaging. Angew Chem Int Ed 49(22):3834–3838. doi:10.1002/anie.200905559

10. Hoelscher D, Shroff R, Knop K, Gottschaldt M, Crecelius A, Schneider B, Heckel DG, Schubert US, Svatos A (2009) Matrix-free UV-laser desorption/ionization (LDI) mass spectrometric imaging at the single-cell level: distribution of secondary metabolites of Arabidopsis thaliana and Hypericum species. Plant J 60(5):907–918. doi:10.1111/j.1365-313X.2009.04012.x
11. Zavalin A, Yang J, Caprioli R (2013) Laser beam filtration for high spatial resolution MALDI imaging mass spectrometry. J Am Soc Mass Spectrom 24(7):1153–1156. doi:10.1007/s13361-013-0638-5
12. Zavalin A, Yang J, Haase A, Holle A, Caprioli R (2014) Implementation of a Gaussian beam laser and aspheric optics for high spatial resolution MALDI imaging MS. J Am Soc Mass Spectrom 25(6):1079–1082. doi:10.1007/s13361-014-0872-5
13. Kettling H, Vens-Cappell S, Soltwisch J, Pirkl A, Haier J, Muething J, Dreisewerd K (2014) MALDI mass spectrometry imaging of bioactive lipids in mouse brain with a Synapt G2-S mass spectrometer operated at elevated pressure: improving the analytical sensitivity and the lateral resolution to ten micrometers. Anal Chem 86(15): 7798–7805. doi:10.1021/ac5017248
14. Thiery-Lavenant G, Zavalin AI, Caprioli RM (2013) Targeted multiplex imaging mass spectrometry in transmission geometry for subcellular spatial resolution. J Am Soc Mass Spectrom 24(4):609–614. doi:10.1007/s13361-012-0563-z
15. Zavalin A, Todd EM, Rawhouser PD, Yang J, Norris JL, Caprioli RM (2012) Direct imaging of single cells and tissue at sub-cellular spatial resolution using transmission geometry MALDI MS. J Mass Spectrom 47(11):1473–1481. doi:10.1002/jms.3108
16. Jurchen JC, Rubakhin SS, Sweedler JV (2005) MALDI-MS imaging of features smaller than the size of the laser beam. J Am Soc Mass Spectrom 16(10):1654–1659. doi:10.1016/j.jasms.2005.06.006
17. Perrot-Rechenmann C, Joannes M, Squalli D, Lebacq P (1989) Detection of phosphoenolpyruvate and ribulose 1,5-bisphosphate carboxylase transcripts in maize leaves by in situ hybridization with sulfonated cDNA probes. J Histochem Cytochem 37(4):423–428
18. Majeran W, Cai Y, Sun Q, van Wijk KJ (2005) Functional differentiation of bundle sheath and mesophyll maize chloroplasts determined by comparative proteomics. Plant Cell Online 17(11):3111–3140. doi:10.1105/tpc.105.035519
19. Korte AR, Lee YJ (2014) MALDI-MS analysis and imaging of low molecular weight metabolites with 1,5-diaminonaphthalene (DAN). J Mass Spectrom 49(8):737–741
20. Korte A, Yagnik G, Feenstra A, Lee Y (2015) Multiplex MALDI-MS imaging of plant metabolites using a hybrid MS system. In: He L (ed) Mass spectrometry imaging of small molecules, vol 1203, Methods in Molecular Biology. Springer, New York, pp 49–62. doi:10.1007/978-1-4939-1357-2_6
21. Strupat K, Kovtoun V, Bui H, Viner R, Stafford G, Horning S (2009) MALDI produced ions inspected with a linear ion trap-Orbitrap hybrid mass analyzer. J Am Soc Mass Spectrom 20(8):1451–1463. doi:10.1016/j.jasms.2009.04.013
22. Lundgren MR, Osborne CP, Christin P-A (2014) Deconstructing Kranz anatomy to understand C4 evolution. J Exp Bot. doi:10.1093/jxb/eru186
23. Fabre N, Rustan I, de Hoffmann E, Quetin-Leclercq J (2001) Determination of flavone, flavonol, and flavanone aglycones by negative ion liquid chromatography electrospray ion trap mass spectrometry. J Am Soc Mass Spectrom 12(6):707–715. doi:10.1016/s1044-0305(01)00226-4
24. Turgeon R (2006) Phloem loading: how leaves gain their independence. Bioscience 56(1):15–24. doi:10.1641/0006-3568(2006)056[0015:plhlgt]2.0.co;2
25. Fraser CM, Chapple C (2011) The phenylpropanoid pathway in Arabidopsis. Arabidopsis Book 9:e0152. doi:10.1199/tab.0152
26. Vermerris W, Nicholson R (2006) Phenolic compound biochemistry. Springer, Dordrecht
27. Rector BG, Liang G, Guo Y (2003) Effect of maysin on wild-type, deltamethrin-resistant, and Bt-resistant Helicoverpa armigera (Lepidoptera: Noctuidae). J Econ Entomol 96(3):909–913
28. Casati P, Walbot V (2005) Differential accumulation of maysin and rhamnosylisoorientin in leaves of high-altitude landraces of maize after UV-B exposure. Plant Cell Environ 28(6):788–799. doi:10.1111/j.1365-3040.2005.01329.x
29. Suzuki T, Kim S-J, Yamauchi H, Takigawa S, Honda Y, Mukasa Y (2005) Characterization of a flavonoid 3-O-glucosyltransferase and its activity during cotyledon growth in buckwheat (Fagopyrum esculentum). Plant Sci 169(5):943–948. doi:10.1016/j.plantsci.2005.06.014
30. Sato N (2004) Roles of the acidic lipids sulfoquinovosyl diacylglycerol and phosphatidylglycerol in photosynthesis: their specificity and evolution. J Plant Res 117(6):495–505. doi:10.1007/s10265-004-0183-1
31. Roughan PG (1985) Phosphatidylglycerol and chilling sensitivity in plants. Plant Physiol 77(3):740–746
32. Kenrick JR, Bishop DG (1986) The fatty acid composition of phosphatidylglycerol and sulfoquinovosyldiacylglycerol of higher plants in relation to chilling sensitivity. Plant Physiol 81(4):946–949
33. Nishihara M, Yokota K, Kito M (1980) Lipid molecular species composition of thylakoid membranes. Biochim Biophys Acta 617(1):12–19
34. Glauser G, Marti G, Villard N, Doyen GA, Wolfender J-L, Turlings TCJ, Erb M (2011) Induction and detoxification of maize 1,4-benzoxazin-3-ones by insect herbivores. Plant J 68(5):901–911. doi:10.1111/j.1365-313X.2011.04740.x
35. Frey M, Chomet P, Glawischnig E, Stettner C, Grun S, Winklmair A, Eisenreich W, Bacher A, Meeley RB, Briggs SP, Simcox K, Gierl A (1997) Analysis of a chemical plant defense mechanism in grasses. Science 277(5326):696–699. doi:10.1126/science.277.5326.696
36. Meihls LN, Handrick V, Glauser G, Barbier H, Kaur H, Haribal MM, Lipka AE, Gershenzon J, Buckler ES, Erb M, Koellner TG, Jander G (2013) Natural variation in maize aphid resistance is associated with 2,4-dihydroxy-7-methoxy-1,4-benzoxazin-3-one glucoside methyltransferase activity. Plant Cell 25(6):2341–2355. doi:10.1105/tpc.113.112409
37. Sicker D, Frey M, Schulz M, Gierl A (2000) Role of natural benzoxazinones in the survival strategy of plants. In: Kwang WJ (ed) International review of cytology, vol 198. Academic Press, p 319–346. doi:10.1016/S0074-7696(00)98008-2
38. Barber J, Gounaris K (1986) What role does sulpholipid play within the thylakoid membrane? Photosynth Res 9(1–2):239–249. doi:10.1007/bf00029747